of water, whereas the pure MgO-periclase coexisting with $MgSiO_3$-perovskite and melt can contain only ~2 ppm H_2O (*16*). Magnesiowüstite is likely to include some Fe^{3+} (*27*). The coupled substitution $2M^{2+} = Fe^{3+} + H^+$ may be necessary to incorporate hydrogen in this phase. Ca-perovskite is a major carrier of trace elements in the lower mantle (*28*). Our study shows that Ca-perovskite has a higher solubility of H_2O than the other two phases. However, the analyses were made after Ca-perovskite became amorphous at ambient pressure, so further investigation on its H_2O solubility with a perovskite structure is needed.

Our results suggest that the lower mantle can potentially store considerable amounts of water. A lower mantle, consisting of 79 wt% Mg-perovskite, 16 wt% magnesiowüstite, and 5 wt% Ca-perovskite (*11*), can contain 0.2 wt% H_2O. When this capacity is integrated over the mass of the lower mantle, the total mass of water is ~5 times that of oceans. This amount is comparable to that in the transition zone (~6 times more than the oceans), where 3.3 and 2.2 wt% H_2O can be included in wadsleyite and ringwoodite, respectively (*5*, *7*). The considerable amount of hydrogen can be stored in deep reservoirs such as the transition zone, lower mantle, and core (*5*–*8*).

The high solubility of H_2O in representative lower mantle minerals also has implications for the rheological properties of the lower mantle (*29*). The presence of water in a crystal structure can reduce the strength of a mineral and control creep mechanisms (*2*, *6*). The water may be transported into the lower mantle by the subduction of hydrated slabs, and may be released upon decomposition of DHMS phases such as phase D, which contains ~10 wt% H_2O, around 1200 km depth (*9*). Hydrogen may be also added to the lower mantle from the hydrogen-saturated outer core as H_2O (*8*). Lower mantle minerals would absorb this released H_2O and would be considerably softened due to the relaxation around the defects. Accordingly, flow of material would be expected along the down-going slabs and along the bottom of the mantle.

References and Notes

1. A. E. Ringwood, *Geochem. J.* **11**, 111 (1977).
2. S. Karato, M. S. Paterson, J. D. FitzGerald, *J. Geophys. Res.* **91**, 8151 (1986).
3. H. Iwamori, *Earth Planet. Sci. Lett.* **160**, 65 (1998).
4. T. Kawamoto, R. L. Herving, J. R. Holloway, *Earth Planet. Sci. Lett.* **142**, 58 (1996).
5. T. Inoue, H. Yurimoto, Y. Kudoh, *Geophys. Res. Lett.* **22**, 117 (1995).
6. D. L. Kohlstedt, H. Keppler, D. C. Rubie, *Contrib. Mineral. Petrol.* **123**, 345 (1996).
7. T. Inoue, D. J. Weidner, P. A. Northrup, J. B. Parise, *Earth Planet. Sci. Lett.* **160**, 107 (1998).
8. T. Okuchi, *Science* **278**, 1781 (1997).
9. S. R. Shieh, H. K. Mao, R. J. Hemley, L. C. Ming, *Earth Planet. Sci. Lett.* **159**, 13 (1998).
10. S. E. Kesson, J. D. Fitz Gerald, J. M. Shelley, *Nature* **393**, 252 (1998).
11. B. J. Wood, *Earth Planet. Sci. Lett.* **174**, 341 (2000).
12. A. Navrotsky, *Science* **284**, 1788 (1999).
13. C. McCammon, *Nature* **387**, 694 (1997).
14. J. P. Brodholt, *Nature* **407**, 620, (2000).
15. C. Meade, J. A. Reffner, E. Ito, *Science* **264**, 1558, (1994).
16. N. Bolfan-Casanova, H. Kepler, D. C. Rubie, *Earth Planet. Sci. Lett.* **182**, 209 (2000).
17. D. R. Bell, G. R. Rossman, *Science* **255**, 1391 (1992).
18. K. Hirose, Y. Fei, S. Ono, T. Yagi, K. Funakoshi, *Earth Planet. Sci. Lett.* **184**, 567 (2001).
19. On SIMS analysis (Cameca ims-3F), a primary ion beam consisted of mass-filtered $^{16}O^-$, accelerated −12.5 kV, with a beam current of about 5 nA and a spot size of 10 to ~15 μm in diameter. Secondary ions were accelerated at 4.5 kV. The intensity of the positive secondary $^1H^+$, $^{30}Si^+$, $^{26}Mg^+$, and $^{44}Ca^+$ ions were measured under steady state secondary ion emissions. To reduce the background signals, the vacuuming level of the sample chamber was maintained at 0.2 μPa, and a cold trap by liquid nitrogen was employed. The samples were coated with Au film of ~20 nm thickness to eliminate electrostatic charging. Two standard materials were measured repeatedly in every analysis of the sample. Accordingly, the calibration lines were constructed with each analysis. Other analytical and instrumental conditions were similar to previous works (*20*, *21*).
20. H. Yurimoto, M. Kurosawa, S. Sueno, *Geochim. Cosmochim. Acta* **53**, 751 (1989).
21. I. Miyagi, H. Yurimoto, *Bull. Volcanol. Soc. Jpn.* **40**, 349 (1995).
22. The counting time of SIMS analysis by one cycle was 2 seconds for $^{30}Si^+$, $^{26}Mg^+$, and $^{44}Ca^+$ ions, and was 10 s for $^1H^+$ ion. All the samples were measured by 250 cycles. Before measurement, pre-sputtering was set at about 100 cycles to obtain a steady state of hydrogen intensity.
23. In the IR study, the IR light emitted by a light source through a Ge-coated KBr beam splitter is focused on a sample by means of Cassegrain mirrors with a magnification of 16. This light passes through a sample, to a MCT (HgCdTe) detector. Several hundreds to thousands scans were accumulated with 4 cm^{-1} resolution to obtain IR absorption spectra of the sample.
24. S. Nakashima *et al.*, *Tectonophysics* **245**, 263 (1995).
25. R. D. Aines, G. R. Rossman, *J. Geophys. Res.* **89**, 4059 (1984).
26. Beer-Lambert law can be expressed as $A_i = ct\varepsilon_i$, where A_i is integrated absorbance, c is molar concentrations of hydrogen, t is the thickness of the sample, and ε_i is the integrated molar absorption coefficient calculated from the method described in (*30*). The error in this estimation is predominantly influenced by ε_i, t, and the anisotropy of the mineral. We adopted the orientation factor ($\zeta = 1/3$).
27. D. J. Frost, F. Langenhorst, P. A. van Aken, *Phys. Chem. Minerals* **28**, 455 (2001).
28. W. Wang, T. Gasparik, R. P. Rapp, *Earth Planet. Sci. Lett.* **181**, 291 (2000).
29. Q. Williams, R. J. Hemley, *Annu. Rev. Earth Planet. Sci.* **29**, 365 (2001).
30. E. Libowitzky and G. R. Rossman, *Am. Mineral.* **82**, 1111 (1997).

31. We thank E. Takahashi, S. Maruyama, and B. F. Windley for discussions and comments, and T. Kawamoto for providing gel starting material. We are grateful to I. Katayama for help with the infrared measurements. TEM analyses were performed at the University of Tokyo.

5 September 2001; accepted 5 February 2002

Repeated and Sudden Reversals of the Dipole Field Generated by a Spherical Dynamo Action

Jinghong Li,[1]* Tetsuya Sato,[1,2]† Akira Kageyama[1,2]

Using long-duration, three-dimensional magnetohydrodynamic simulation, we found that the magnetic dipole field generated by a dynamo action in a rotating spherical shell repeatedly reverses its polarity at irregular intervals (that is, punctuated reversal). Although the total convection energy and magnetic energy alternate between a high-energy state and a low-energy state, the dipole polarity can reverse only at high-energy states where the north-south symmetry of the convection pattern is broken and the columnar vortex structure becomes vulnerable. Another attractive finding is that the quadrupole mode grows, exceeding the dipole mode before the reversal; this may help to explain how Earth's magnetic field reverses.

Earth's magnetic field is believed to be generated by dynamo action in a rotating electrically conducting fluid (*1*–*3*). The magnetic field of Earth is dipole-dominated and suddenly reverses its polarity at irregular intervals (*4*, *5*).

Three-dimensional magnetohydrodynamic simulations in recent years have succeeded in demonstrating the self-excitation of the dipole field (*6*–*8*). In the Glatzmaier-Roberts simulation (*6*), reversal of the generated dipole field was also observed. On the other hand, the Kageyama-Sato model obtained a flip-flop transition of the total magnetic and convection energies, which was associated with the reversal of the dipole field (*9*). Glatzmaier *et al.* (*10*) studied the effects of nonuniformity of heat flux pattern on the reversal to find the role of the nonuniform heat flux. Coe *et al.* (*11*) described the evolution of the morphology and/or spectral energy of simulated magnetic fields during reversals. Although the previous reversal studies have succeeded in demonstrating the occurrence

[1]Department of Fusion Science, The Graduate University for Advanced Studies, Toki, 509-5292, Japan. [2]Theory and Computer Simulation Center, National Institute for Fusion Science, Toki, 509-5292, Japan.

*Permanent address: Institute of Applied Physics and Computational Mathematics, Post Office Box 8009, Beijing 100088, China.

†To whom correspondence should be addressed. E-mail: sato@tcsc.nifs.ac.jp

of reversal and in finding circumstantial conditions during reversal, they have not elucidated the physical mechanism that directly causes the reversal.

Following the Kageyama-Sato model (*7*–*9*), we studied the three-dimensional evolution of the thermal convection and the magnetic field in an electrically conductive rotating spherical fluid shell. An ideal gas approximation is used for the fluid. The inner boundary of radius r_i and outer boundary of radius r_o of the spherical shell are kept at constant temperatures of T_i and T_o, respectively (where $T_i > T_o$). Gravity and the temperature difference drive the thermal convection. No-slip boundary conditions are imposed on both boundaries, and the magnetic field at the boundaries is assumed to be normal to the boundaries.

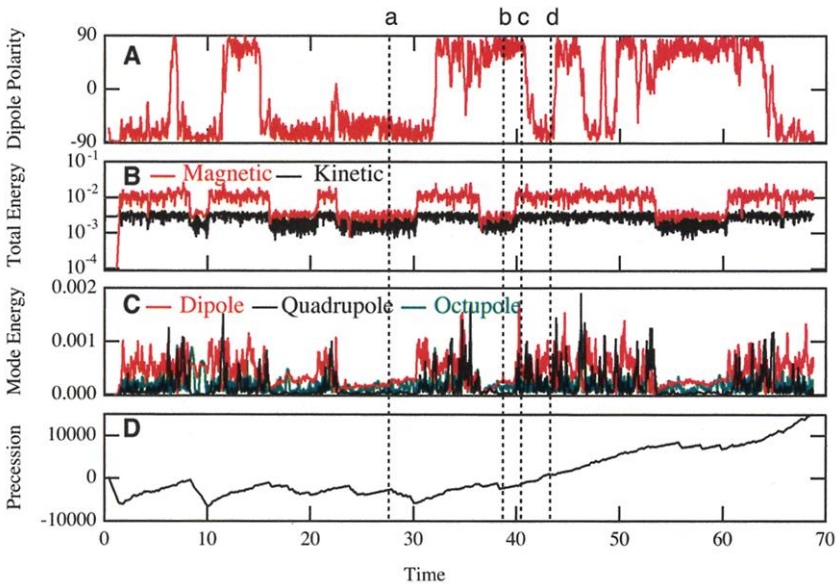

Fig. 1. Time evolutions of (**A**) the polarity of dipole field (expressed by pole latitude in degrees), (**B**) the total kinetic (black) and magnetic (red) energies, (**C**) the mean magnetic energy densities of the dipole (red), the quadrupole (black), and octupole (green) modes at the outer boundary, and (**D**) the precession, expressed in degrees, of magnetic dipole moment.

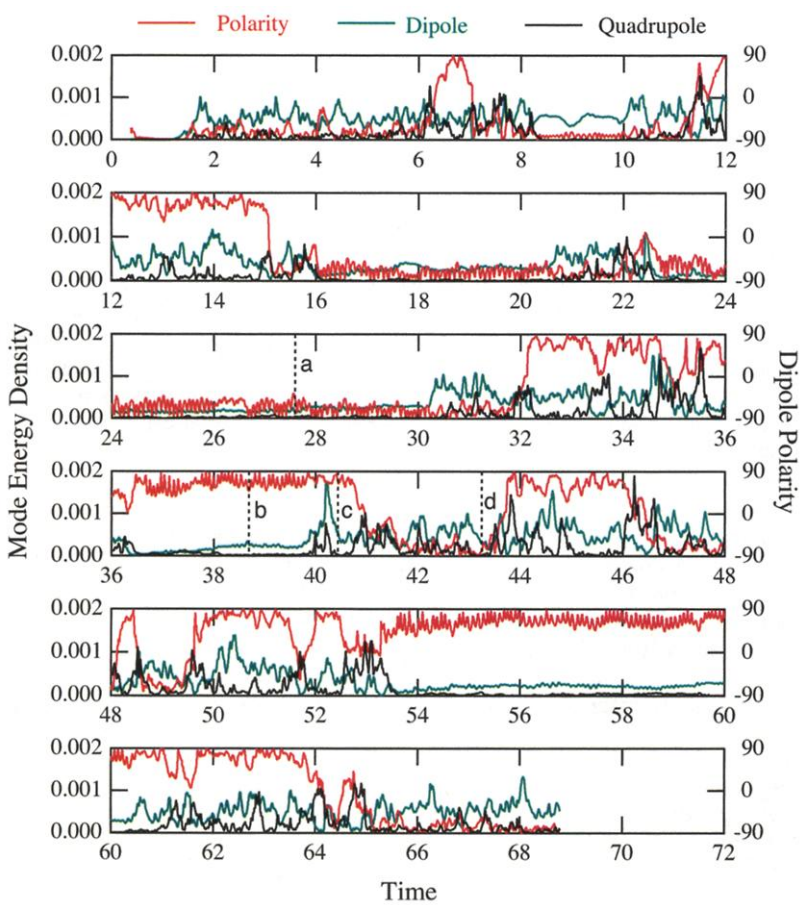

Fig. 2. Detailed time correlation between the dipole polarity (red) and the magnetic energy densities of the dipole (green) and the quadrupole (black) modes.

We have made many simulations by varying the electrical resistivity, the temperature difference between the inner and outer boundaries, and the angular velocity of rotation. In this study, we concentrate on one representative long-term behavior of the dipole reversal. The parameters are as follows: The ratio of inner and outer radius is $r_i:r_o = 0.3$, the Taylor number is 5.88×10^6, the modified Rayleigh number is 3.36×10^4, the Prandtl number is 1.0, and the magnetic Prandtl number is 10.5. The characteristic nondimensional numbers of the present simulation are as follows: The magnetic Reynolds number is 3.4×10^2. Rossby and kinetic Reynolds numbers are 1.3×10^{-2} and 32. The electromagnetic diffusion time is adopted as the unit of time scale. We see a dipole field reversal that is irregular and rapidly reversing (Fig. 1A), and the reversal period is roughly on the order of 10 diffusion times.

The total magnetic and kinetic energies (Fig. 1B) exhibit an alternation between a high-energy state and a low-energy state (*9*), and the reversal occurs only at a high-energy state. Furthermore, the simulations show that reversal can occur when a high-energy state continues for a duration of more than twice the electromagnetic diffusion time. This tendency is clearly recognized in the relatively short-lived high-energy state, starting at about time = 20.5. In this high-energy state, the magnetic field should reverse but it does not. The reversal was interrupted by a transition from the high-energy state to the low-energy state. Upon examining our long-run simulations for varying parameter set, the previous simulation (*9*), where the field reversal occurred in accordance with energy transition, turns out to be a very rare case. In fact, we found that the previous reversal (*9*) was only transient and the system eventually relaxed to a steady state.

The time evolution of the three dominant magnetic harmonic modes at the outer boundary (Fig. 1C) shows that the dipole reversal always occurs when the magnitude of the quadrupole mode exceeds that of the dipole mode. In order to see the relationship between the dipole reversal and the behavior of the quadrupole mode in more detail, we plotted its evolution on a finer scale in Fig. 2. The quadrupole mode is found to grow before the reversal and becomes the dominant mode

while the reversal is developing. These results suggest that the magnetic field reversal is correlated with the growth and dominance of the quadrupole mode. We note that the Glatzmaier-Roberts simulation (*10*) also observed tendencies similar to this. The precession of the tip of the dipole moment around the rotation axis (Fig. 1D) shows that the precession is, as a whole, eastward at the high-energy state and westward at the low-energy state, but that there seems to be no correlation with the dipole reversal. The magnetic field configurations just before and after one of the dipole reversals (Fig. 3) shows the dipole polarity change in the range of 6 to 16 diffusion times.

The thermal convection in the rapidly rotating spherical shell takes the form of columnar cells which are parallel to the rotation axis (*8*). The fluid in a cyclonic (anticyclonic) column rotates in the same (opposite) direction as the rotation of the shell. The flow in a cyclonic (anticyclonic) column is directed toward (away from) the equatorial plane. The magnetic field structure inside the shell is complicated; generally, the magnetic field lines spiral around the convection columns. The magnetic field pattern at the outer boundary moves eastward at high-energy states and westward at low-energy states.

At low-energy states, the thermal convection motion does not change very much, and seven pairs of convection columns simply drift in longitude with fast speed (about 0.5% of the angular velocity of rotation). The fluid flow is generally symmetric about the equatorial plane (i.e., north-south symmetry) and there are no flows across the equatorial plane (see the left two panels of top two rows in Fig. 4). The magnetic field is always dominantly dipolar and the dipole moment suffers only a small fluctuation in magnitude (less than 10%) and direction.

In contrast, at high-energy states, the number of convection column pairs (i.e., cyclone and anticyclone) is not fixed, changing among five to seven pairs. Meanwhile, strong trans-equatorial flows, which are comparable to or even greater than the mean poloidal flow, develop and the symmetry of the convection pattern around the equatorial plane is broken (see the left two panels of bottom two rows in Fig. 4). It is this break of north-south symmetry in the flow pattern that drives the turn-over of the polarity of dipole.

The properties of magnetic field at high-energy states in the equatorial and meridian planes show that the axial magnetic fields across the equatorial plane are mainly concentrated in the anticyclone columns. Also, it should be noted that the toroidal contour pattern of the longitudinally averaged magnetic field in the meridian cross section is reversed as the dipole polarity is reversed (compare the upper two rows of the righthand

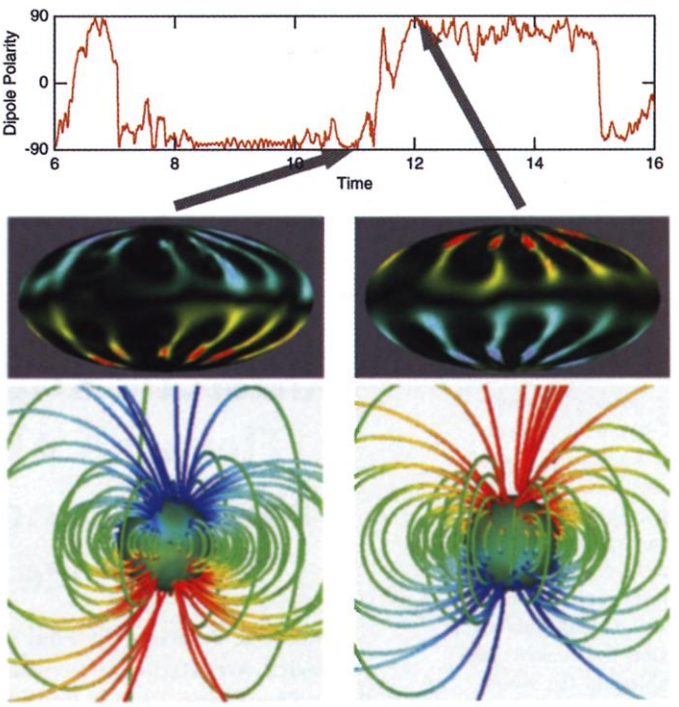

Fig. 3. Two snapshots of the generated magnetic fields before and after a reversal. The top panel indicates the magnified time evolution of the dipole polarity in the range of 6 to 16 diffusion times. The middle panels show the color-coded representation of the radial component at the outer boundary of the dynamo shell (red directed outward and blue inward). The bottom panels show the magnetic field lines extending out of the shell before (time = 11.0) and after (time = 12.0) the reversal around time = 11.5, where the direction of a magnetic field line is color-coded by red to blue for outward and inward directions, respectively.

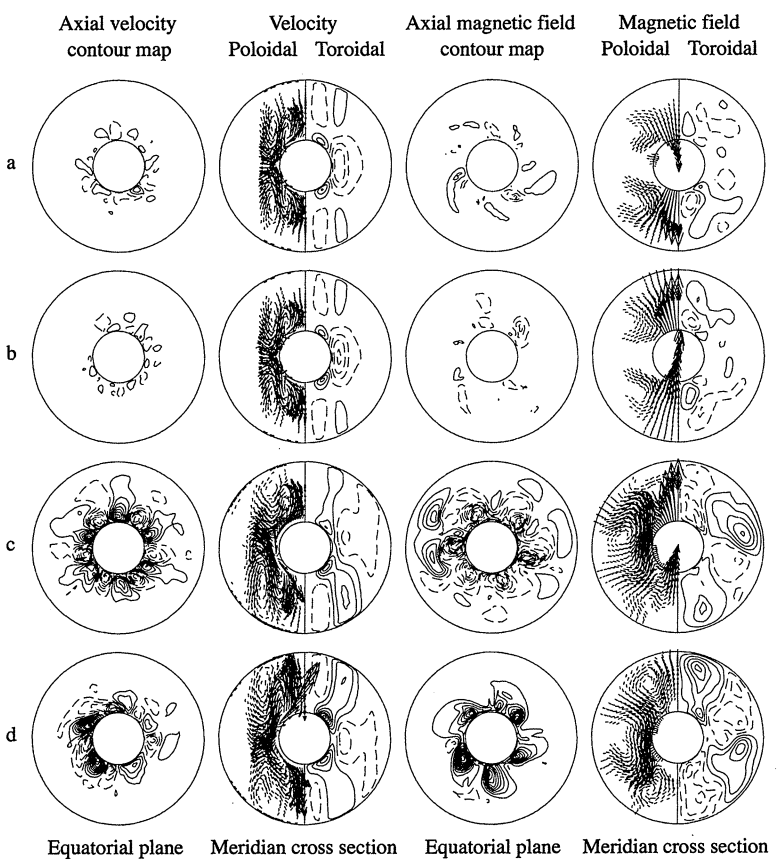

Fig. 4. The contour maps of axial components of fluid velocity and magnetic field in the equatorial plane are shown on the first and third columns, where solid lines represent south-directed and dashed ones north-directed. Shown on the second and fourth columns are the longitudinally averaged fluid velocity and magnetic field vector in the meridian cross section, where the left half represents the poloidal component and the right half the contour map of the toroidal component (solid lines represent east-directed and dashed ones west-directed). Rows (**A**) through (**D**) correspond to the times indicated in Figs. 1 and 2. Namely, the states (A) and (D) represent the normal polarity and those of (B) and (C) the reversal polarity.

side in Fig. 4, and also the lower two rows in Fig. 4).

The energy state, both magnetic and kinetic, of a magnetohydrodynamic dynamo in a rotating spherical shell has two local minima, namely, the dynamo system can alternately take a high- or low-energy state. More specifically, the system flip-flops in an irregular fashion between a high- and a low-energy state. A reversal occurs only in a high-energy state and only if the high-energy state is maintained for a certain period. More interestingly, there appears a rather gradual growth phase of the quadrupole mode before a reversal, and a reversal occurs when the magnitude of the quadrupole mode exceeds that of the dipole at the outer boundary. Note, however, that when an observer measures the quadrupole component on Earth's surface, this is not the case because the quadrupole mode amplitude decreases much faster than that of the dipole as the radial distance increases.

The most important discovery of these simulations is the generation of trans-equatorial flows in a spherical system that makes the convection pattern vulnerable and the whole system marginally stable. Reversal of the dipole magnetic field arises with a good correlation with the generation of trans-equatorial flows. We remind here that Sarson and Jone (*12*) and Sarson (*13*) have made an argument on the importance of nonaxisymmetric poloidal flow on the reversal.

The necessary conditions for the occurrence of a dipole reversal obtained in our model are the following: (i) The system is in a high-energy state, (ii) the high-energy state lasts for a certain period, (iii) the quadrupole mode is on the average in a growing phase, and (iv) the magnitude of the quadrupole mode exceeds that of the dipole mode on the outer boundary. The last two conditions are consistent with the suggested correlations between field strengths and reversals (*14*). Although the parameter region of the real Earth is far from the present one, we believe that the core mechanism of the dipole reversal must be a universal one, as is often the case for most phenomena in nature, and that the elementary reversal mechanism could be the generation of the north-south asymmetric flow. This is because the flow pattern is the only direct agency related to the magnetic field pattern. Furthermore, other simulation runs have disclosed that the energy state always stays in a high-energy state for larger Rayleigh numbers. In Earth's case, the Rayleigh number is much higher than those of our simulation examples. Thus, it is quite likely that reversal can take place in the real Earth.

References

1. H. K. Moffatt, *Magnetic Field Generation in Electrically Conducting Fluids* (Cambridge Univ. Press, Cambridge, 1978).
2. P. H. Roberts, A. M. Soward, *Annu. Rev. Fluid Mech.* **24**, 459 (1992).
3. P. H. Roberts, G. A. Glatzmaier, *Rev. Mod. Phys.* **72**, 1081 (2000).
4. J. A. Jacobs, *Reversals of the Earth's Magnetic Field* (Cambridge Univ. Press, Cambridge, ed. 2, 1994).
5. R. T. Merrill, M. W. McElhinny, P. L. McFadden, *The Magnetic Field of the Earth: Paleomagnetism, the Core, and the Deep Mantle* (Academic Press, San Diego, CA, 1996).
6. G. A. Glatzmaier, P. H. Roberts, *Nature* **377**, 203 (1995).
7. A. Kageyama, T. Sato, The Complexity Simulation Group, *Phys. Plasmas* **2**, 1421 (1995).
8. ———, *Phys. Rev. E* **55**, 4617 (1997).
9. A. Kageyama, M. M. Ochi, T. Sato, *Phys. Rev. Lett.* **82**, 5409 (1999).
10. G. A. Glatzmaier, R. S. Coe, L. Hongre, P. H. Roberts, *Nature* **401**, 885 (1999).
11. R. S. Coe, L. Hongre, G. A. Glatzmaier, *Philos. Trans. R. Soc. London Ser. A* **358**, 1141 (2000).
12. G. R. Sarson, C. A. Jones, *Phys. Earth Planet. Inter.* **111**, 3 (1999).
13. G. R. Sarson, *Philos. Trans. R. Soc. London Ser. A* **358**, 921 (2000).
14. A. Cox, *J. Geophys. Res.* **73**, 3247 (1968).

9 October 2001; accepted 4 February 2002

Antarctic Krill Under Sea Ice: Elevated Abundance in a Narrow Band Just South of Ice Edge

Andrew S. Brierley,[1]*† Paul G. Fernandes,[2] Mark A. Brandon,[3] Frederick Armstrong,[2] Nicholas W. Millard,[4] Steven D. McPhail,[4] Peter Stevenson,[4] Miles Pebody,[4] James Perrett,[4] Mark Squires,[4] Douglas G. Bone,[1] Gwyn Griffiths[4]

We surveyed Antarctic krill (*Euphausia superba*) under sea ice using the autonomous underwater vehicle *Autosub-2*. Krill were concentrated within a band under ice between 1 and 13 kilometers south of the ice edge. Within this band, krill densities were fivefold greater than that of open water. The under-ice environment has long been considered an important habitat for krill, but sampling difficulties have previously prevented direct observations under ice over the scale necessary for robust krill density estimation. *Autosub-2* enabled us to make continuous high-resolution measurements of krill density under ice reaching 27 kilometers beyond the ice edge.

Antarctic krill (*Euphausia superba*) is a key species in the Southern Ocean and depends on sea-ice algae for food at some stages of its life cycle (*1*). Interannual changes in the recruitment success of krill have been linked to oscillations in sea-ice extent, and krill abundance may decline following successive winters of reduced ice coverage (*2*). Reductions in krill abundance have major consequences throughout the Southern Ocean ecosystem (*3*) and affect commercial fisheries (*4*), and it is essential to understand interactions of krill with sea ice. In summer, the marginal ice zone (MIZ), where melting sea ice is broken into floes by waves and swell, is a region of elevated primary productivity (*5*). Phytoplankton blooms develop in the upper water column that is stabilized by melt-water, and krill may feed on these blooms. It has long been presumed that krill abundance is elevated along sea-ice edges because some krill-eating whales aggregate there (*6*). However, although krill swarms have been seen in open water between sea-ice floes (*7*) and discrete spot-measurements have detected krill under ice (*8–11*), there is a paucity of quantitative information on the mesoscale distribution and abundance of krill beneath ice because of difficulties associated with sampling there. Limitations with conventional methods have prevented continuous observations beneath ice over the scale necessary to assess krill robustly: ice-breaking ships disrupt the sea-ice habitat, and scuba divers and remotely operated vehicles suffer restricted operating ranges. Evidence for krill–sea ice links thus remains largely circumstantial (*2*). Here, we report acoustic survey data gathered along replicated line-transects by the autonomous underwater vehicle (AUV) *Autosub-2* (*12*) during its first missions beneath sea ice. These data enable krill density and distribu-

[1]British Antarctic Survey, High Cross, Madingley Road, Cambridge CB3 0ET, UK. [2]Fisheries Research Services (FRS) Marine Laboratory Aberdeen, Post Office Box 101, Victoria Road, Aberdeen, AB11 9DB, UK. [3]The Open University, Department of Earth Sciences, Walton Hall, Milton Keynes, MK7 6AA, UK. [4]Southampton Oceanography Centre, Empress Dock, Southampton SO14 3ZH, UK.

*To whom correspondence should be addressed. E-mail: andrew.brierley@st-andrews.ac.uk

†Present address: Gatty Marine Laboratory, University of St. Andrews, Fife, KY16 8LB, UK.